Study on PWM Rectifier Without Grid Voltage Sensor Based on Virtual Flux Delay Compensation Algorithm

Hui Zhang, Xiaoxiao Zhu, Jingcong Shi, Li Tan, Chuanjin Zhang, and Kun Hu

***Abstract*—At present, virtual flux voltage oriented control strategy is one of the widely used control strategies without grid voltage sensor. To solve the dc bias resulting from voltage vector integration in vector calculation of virtual flux and further avoid the steady-state error, a virtual flux observer with negative feedback resonant filter is presented in this paper based on virtual flux principle and a delay compensation algorithm is also proposed to solve the delay of virtual flux. In addition, the control system diagram of the pulsewidth modulated rectifier without grid voltage sensor is brought forth. Then, simulation system and experimental platform are both established to simulate and test the rectifier. Eventually, the correctness and feasibility of the proposed algorithm are verified through the analysis of simulation and experimental results.**

***Index Terms*—Pulsewidth modulated (PWM) rectifier, sensorless, virtual flux.**

I. Introduction

As THE widely used power electronic equipment, pulsewidth modulated (PWM) rectifier has long been the research hotspot. The algorithm without grid voltage sensor has irreplaceable advantages over various rectifier systems. Through the algorithm without grid voltage sensor, both volume and cost can be reduced, which has great significance for low power system with compact structure [1]–[3]. There are various control strategies without grid voltage sensor [4]–[6], among which, virtual flux-oriented control (VFOC) strategy [7]–[10] is most widely used. This control strategy comprises two parts; one is grid voltage amplitude and phase observation, and the other one is double closed-loop control in the synchronous rotating coordinate system. Since double closed-loop control is the same as traditional voltage oriented control (VOC) strategy, the current

Manuscript received July 22, 2017; revised January 7, 2018; accepted February 23, 2018. Date of publication March 11, 2018; date of current version November 19, 2018. This work was supported by the Fundamental Research Funds for the Central Universities 2018QNB03. Recommended for publication by Associate Editor B. Wang. *(Corresponding author: Kun Hu.)*

H. Zhang, X. Zhu, L. Tan, and K. Hu are with the School of Electrical and Power Engineering, China University of Mining and Technology, Xuzhou 221116, China (e-mail:

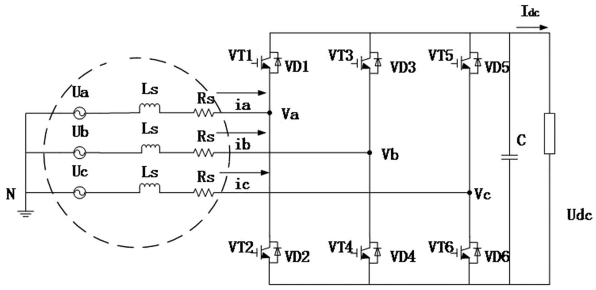

Fig. 1. Main circuit of PWM rectifier.

with low-pass filter compensation link is proposed to precis the flux observer in VFOC of the PWM rectifier. Low-pass filter adopted in conventional virtual grid flux to substitute the pure integrator to least the dc drift would result in error of amplitude and phase angle. Although flux observation results no longer rely on the initial value, the amplitude and phase errors still exist [26]. In [27], a new control strategy for three-level neutral point clamped PWM rectifier without power source voltage sensors is presented. Virtual flux is estimated and used to calculate the phase of the power source voltage and instantaneous power. Then, on these bases, a direct power control scheme for three-level PWM rectifier is presented. An optimal switching table is established and vector switching scheme and balance strategy for the neutral point potential are discussed. But the calculation is complicated, which increases the operation difficulty. In [28], a control strategy for PWM rectifiers without grid voltage sensor employing a current-shaping strategy is proposed. The proposed technique has the ability to reject harmonic components from grid voltage and power factor adaptation in the presence of uncertain grid impedance. Nevertheless, this increases the complexity of the control design once there are more uncertain parameters. For those reasons, the absence of voltage sensors is preferable. In [29], an adaptive algorithm is employed to achieve a high power factor in the grid even for uncertain parameters of the circuit impedance and load power. For the current shaping strategy applied in the control of active filters, none of the solutions, *RC* or PI/PID, are explored for a better disturbance rejection.

In this paper, a virtual flux observer with negative feedback resonant filter is proposed based on the principle of virtual flux, and the derivation process and setting method for parameters of the observer are also presented. As for the time delay problem of virtual flux, a delay compensation algorithm is proposed to adjust virtual flux phase by adjusting the inductance value used for the calculation of virtual flux. The simulation and experiment prove that the proposed method in this paper can avoid steady-state error and show good control performance in the meantime.

II. Virtual Flux Delay Compensation Algorithm Based on Resonant Filter With Negative Feedback

A. Mathematical Model of Virtual Flux Observer

The main circuit of the PWM rectifier is shown in Fig. 1, in which, U_a, U_b, and U_c refer to three-phase grid voltage,

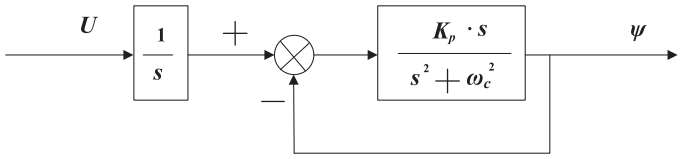

Fig. 2. Resonant filter with negative feedback.

L_s refers to inductance, R_s refers to equivalent resistance of electric reactor and switching loss, $\mathrm{V}_{T1}-\mathrm{V}_{T6}$ are the IGBTs, $\mathrm{V}_{D1}-\mathrm{V}_{D6}$ are the diodes, *C* is the dc-link capacitance, U_{dc} is the dc-side voltage.

The mathematical model of the PWM rectifier in $\alpha\beta$ two-phase static coordinate is expressed as follows:

$$\begin{bmatrix} U_\alpha \\ U_\beta \end{bmatrix} = L\frac{d}{dt}\begin{bmatrix} i_\alpha \\ i_\beta \end{bmatrix} + U_{\mathrm{dc}}\begin{bmatrix} S_\alpha \\ S_\beta \end{bmatrix}. \tag{1}$$

Set

$$\begin{bmatrix} \Psi_\alpha \\ \Psi_\beta \end{bmatrix} = \begin{bmatrix} \int U_\alpha dt \\ \int U_\beta dt \end{bmatrix}. \tag{2}$$

Integrate (1) and combine (2), the definite integration equation in the control system is as follows:

$$\begin{bmatrix} \int_0^t U_\alpha dt \\ \int_0^t U_\beta dt \end{bmatrix} = L\begin{bmatrix} i_\alpha \\ i_\beta \end{bmatrix} + U_{\mathrm{dc}}\begin{bmatrix} \int_0^t S_\alpha dt \\ \int_0^t S_\beta dt \end{bmatrix}. \tag{3}$$

B. Analysis on Characteristics of Resonant Filter With Negative Feedback

DC component generated from integration initial value is included in the integration result of (3), which must be eliminated to accurately calculate the rotation angle of grid voltage vector. For this purpose, an improved negative feedback resonant filter is proposed in this paper.

The structure of the resonant filter with negative feedback is shown in Fig. 2, including pure integration and negative feedback resonant filtering. In this figure, K_p is open-loop gain coefficient of the resonant filter, which can adjust dynamic characteristics of the resonant filter; ω_c is the resonance point. Since the input signal *U* contains ac component of fundamental frequency and dc component generated from integration initial value after the integration, the fundamental frequency is selected as the resonance point of this resonant filter, namely, $\omega_C = \omega_0$.

So the transfer function of the input signal *U* and the output signal Ψ is as follows:

$$\Phi(s) = \frac{K_p}{s^2 + K_p s + \omega_0^2}. \tag{4}$$

The phase change of amplitude of fundamental frequency signal is as follows:

$$\Psi = U\Phi(j\omega_0). \tag{5}$$

The following formula can be derived through simplification of (4) and (5):

$$\Psi = U\frac{1}{j\omega_0} = \frac{U}{\omega_0}e^{-j\frac{\pi}{2}}. \tag{6}$$

So response value equals to theoretical value, namely, $\Psi = \Psi_{\text{theory}}$.

Set

$$\begin{cases} U_\alpha = U_m \sin\left(\omega_0 t + \theta_0 + \frac{\pi}{2}\right) \\ U_\beta = U_m \sin\left(\omega_0 t + \theta_0\right). \end{cases} \tag{7}$$

Then, the expression of U_β in complex frequency domain is as follows:

$$U_\beta(s) = U_m \frac{\omega_0 \cos\theta_0 + s\sin\theta_0}{s^2 + \omega_0^2} \tag{8}$$

and the expression of $\Psi_\beta(s)$ in complex frequency domain is as follows:

$$\Psi_\beta(s) = \frac{U_m}{\omega_0}\left[\begin{array}{c} \dfrac{(s+K_p)\cos\theta_0 - \omega_0\sin\theta_0}{s^2 + K_p s + \omega_0^2} \\ + \dfrac{\omega_0 \cos\left(\theta_0 - \dfrac{\pi}{2}\right) + s\sin\left(\theta_0 - \frac{\pi}{2}\right)}{s^2 + \omega_0^2} \end{array}\right] \tag{9}$$

where steady-state component is the fundamental component

$$\tilde{\Psi}_\beta(s) = \frac{U_m}{\omega_0}\frac{\omega_0 \cos\left(\theta_0 - \frac{\pi}{2}\right) + s\sin\left(\theta_0 - \frac{\pi}{2}\right)}{s^2 + \omega_0^2}. \tag{10}$$

So, the expression of corresponding fundamental component in time domain is as follows:

$$\tilde{\Psi}_\beta(t) = \frac{U_m}{\omega_0}\sin\left(\omega_0 t + \theta_0 - \frac{\pi}{2}\right) \tag{11}$$

where the transient component is as follows:

$$\bar{\Psi}_\beta(s) = \frac{U_m}{\omega_0}\frac{(s+K_P)\cos\theta_0 - \omega_0\sin\theta_0}{s^2 + K_p s + \omega_0^2}. \tag{12}$$

When $K_p = 2\omega_0$, transient component is the same as that in the series algorithm of dual low-pass filter, which is shown as follows:

$$\bar{\Psi}_\beta(t) = \frac{U_m}{\omega_0}\left[\cos\theta_0 + \sqrt{2}\omega_0 t\cos\left(\theta_0 + \frac{\pi}{4}\right)\right]e^{-\omega_0 t}. \tag{13}$$

Similarly, transient component in α-axis is as follows:

$$\bar{\Psi}_\alpha(t) = \frac{U_m}{\omega_0}\left[\cos\theta_0 + \sqrt{2}\omega_0 t\cos\left(\theta_0 + \frac{\pi}{4}\right)\right]e^{-\omega_0 t}. \tag{14}$$

Thus, the square of amplitude of transient component is as follows:

$$\bar{\Psi}^2(t) = \left(\bar{\Psi}_\beta\right)^2(t) + \left(\bar{\Psi}_\alpha\right)^2(t). \tag{15}$$

The following equation can be derived through substitution of (13) and (14) into (15):

$$\bar{\Psi}^2(t) = \left(\frac{U_m}{\omega_0}\right)^2\left[2{\omega_0}^2 t^2 + 2\omega_0 t + 1\right]e^{-2\omega_0 t}. \tag{16}$$

When $K_p > 2\omega_0$, without regard to the exceptional case of pole-zero cancellation, (12) can be further simplified as follows:

$$\bar{\Psi}_\beta(s) = \frac{k_1}{s+s_1} + \frac{k_2}{s+s_2} \tag{17}$$

where

$$s_1 = \frac{K_p + \sqrt{K_p^2 - 4\omega_0^2}}{2},\ s_1 = \frac{K_p - \sqrt{K_p^2 - 4\omega_0^2}}{2}$$

$$k_1 = \frac{\cos\theta_0\left(\sqrt{K_p^2 - 4\omega_0^2} - K_p\right) + 2\omega_0\sin\theta_0}{2\sqrt{K_p^2 - 4\omega_0^2}}$$

$$k_2 = \frac{\cos\theta_0\left(\sqrt{K_p^2 - 4\omega_0^2} - K_p\right) - 2\omega_0\sin\theta_0}{2\sqrt{K_p^2 - 4\omega_0^2}}.$$

Therefore, (15) is expressed in time domain as follows:

$$\bar{\Psi}_\beta(t) = \frac{U_m}{\omega_0} \times \left[\begin{array}{l} \dfrac{\cos\theta_0\left(\sqrt{K_p^2 - 4\omega_0^2} - K_p\right) + 2\omega_0\sin\theta_0}{2\sqrt{K_p^2 - 4\omega_0^2}} \\ \quad \times e^{-\frac{K_P - \sqrt{K_p^2 - 4\omega_0^2}}{2}t} \\ + \dfrac{\cos\theta_0\left(\sqrt{K_p^2 - 4\omega_0^2} - K_p\right) - 2\omega_0\sin\theta_0}{2\sqrt{K_p^2 - 4\omega_0^2}} \\ \quad \times e^{-\frac{K_P - \sqrt{K_p^2 - 4\omega_0^2}}{2}t} \end{array}\right]. \tag{18}$$

Similarly, the transient component in the α-axis is as follows:

$$\bar{\Psi}_\alpha(t) = \frac{U_m}{\omega_0} \times \left[\begin{array}{l} \dfrac{-\sin\theta_0\left(\sqrt{K_p^2 - 4\omega_0^2} - K_p\right) + 2\omega_0\cos\theta_0}{2\sqrt{K_p^2 - 4\omega_0^2}} \\ \quad \times e^{-\frac{K_P - \sqrt{K_p^2 - 4\omega_0^2}}{2}t} \\ + \dfrac{-\sin\theta_0\left(\sqrt{K_p^2 - 4\omega_0^2} - K_p\right) - 2\omega_0\cos\theta_0}{2\sqrt{K_p^2 - 4\omega_0^2}} \\ \quad \times e^{-\frac{K_P - \sqrt{K_p^2 - 4\omega_0^2}}{2}t} \end{array}\right]. \tag{19}$$

So the square of amplitude of the transient component is as follows:

$$\bar{\Psi}^2 = \left(\bar{\Psi}_\beta\right)^2 + \left(\bar{\Psi}_\alpha\right)^2. \tag{20}$$

The following equation can be derived through substitution of (18) and (19) into (20):

$$\bar{\Psi}^2(t) = \left(\frac{U_m}{\omega_0}\right)^2 \times \left[\begin{array}{l} \dfrac{K_p^2 - K_p\sqrt{K_p^2-4\omega_0^2}}{2\left(K_p^2-4\omega_0^2\right)} e^{-\left(K_p+\sqrt{K_p^2-4\omega_0^2}\right)t} \\ +\dfrac{K_p^2 + K_p\sqrt{K_p^2-4\omega_0^2}}{2\left(K_p^2-4\omega_0^2\right)} e^{-\left(K_p-\sqrt{K_p^2-4\omega_0^2}\right)t} \\ +\dfrac{-4\omega_0^2}{K_p^2-4\omega_0^2} e^{-K_p t} \end{array}\right]. \quad (21)$$

When $K_p < 2\omega_0$, (18) can be expressed as follows:

$$\bar{\Psi}_\beta(s) = \frac{U_m}{\omega_0} \frac{k_1\sqrt{\omega_0^2 - \frac{K_p^2}{4}} + k_2\left(s+\frac{K_p}{2}\right)}{\left(s+\frac{K_p}{2}\right)^2 + \left(\omega_0^2 - \frac{K_p^2}{4}\right)} \quad (22)$$

where $k_1 = \frac{K_p\cos\theta_0 - 2\omega_0\sin\theta_0}{\sqrt{4\omega_0^2-K_p^2}}$, $k_2 = \cos\theta_0$. Equation (22) is expressed in time domain as follows:

$$\bar{\Psi}_\beta(t) = \frac{U_m}{\omega_0} \times \left[\begin{array}{l} \dfrac{K_p\cos\theta_0 - 2\omega_0\sin\theta_0}{\sqrt{4\omega_0^2-K_p^2}} \\ \dfrac{\sqrt{4\omega_0^2-K_p^2}}{\sqrt{4\omega_0^2-K_p^2}}\sin\left(\sqrt{\omega_0^2-\dfrac{K_p^2}{4}}t\right) \\ +\cos\theta_0\cos\left(\sqrt{\omega_0^2-\dfrac{K_p^2}{4}}t\right) \end{array}\right] e^{-\frac{K_p}{2}t}. \quad (23)$$

Similarly, transient component in the α-axis is as follows:

$$\bar{\Psi}_\alpha(t) = \frac{U_m}{\omega_0} \times \left[\begin{array}{l} \dfrac{-K_p\sin\theta_0 - 2\omega_0\cos\theta_0}{\sqrt{4\omega_0^2-K_p^2}} \\ \dfrac{\sqrt{4\omega_0^2-K_p^2}}{\sqrt{4\omega_0^2-K_p^2}}\sin\left(\sqrt{\omega_0^2-\dfrac{K_p^2}{4}}t\right) \\ -\sin\theta_0\cos\left(\sqrt{\omega_0^2-\dfrac{K_p^2}{4}}t\right) \end{array}\right] e^{-\frac{K_p}{2}t}. \quad (24)$$

So the square of amplitude of the transient component is as follows:

$$\bar{\Psi}^2(t) = \left(\frac{U_m}{\omega_0}\right)^2 \left[\begin{array}{l} \dfrac{K_p}{\sqrt{4\omega_0^2-K_p^2}}\sin\left(\sqrt{4\omega_0^2-K_p^2}t\right) \\ -\dfrac{-K_p^2}{4\omega_0^2-K_p^2}\cos\left(\sqrt{4\omega_0^2-K_p^2}t\right) \\ +\dfrac{4\omega_0^2}{4\omega_0^2-K_p^2} \end{array}\right] e^{-K_p t}. \quad (25)$$

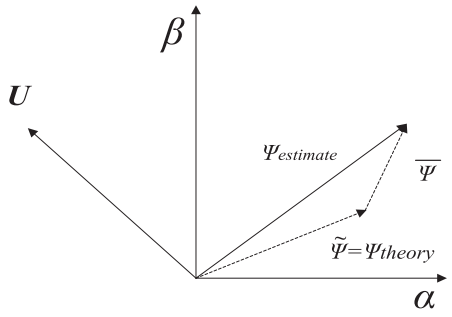

Fig. 3. Virtual flux vector.

TABLE I
SQUARE OF AMPLITUDE OF TRANSIENT COMPONENT WITH DIFFERENT *Kp*

K_p value	Square of amplitude of transient component $\bar{\Psi}^2(t)$
$K_p = 2\omega_0$	$\left(\frac{U_m}{\omega_0}\right)^2\left[2\omega_0^2t^2+2\omega_0t+1\right]e^{-2\omega_0t}$
$K_p > 2\omega_0$	$\left(\frac{U_m}{\omega_0}\right)^2\frac{e^{-K_pt}}{K_p^2-4\omega_0^2}\left[\begin{array}{l}K_p^2\cosh\left(\sqrt{K_p^2-4\omega_0^2}t\right)\\+\left(K_p\sqrt{K_p^2-4\omega_0^2}\right)\sinh\left(\sqrt{K_p^2-4\omega_0^2}t\right)\\-4\omega_0^2\end{array}\right]$
$K_p < 2\omega_0$	$\left(\frac{U_m}{\omega_0}\right)^2\frac{e^{-K_pt}}{K_p^2-4\omega_0^2}\left[\begin{array}{l}K_p^2\cos\left(\sqrt{4\omega_0^2-K_p^2}t\right)\\+\left(K_p\sqrt{4\omega_0^2-K_p^2}\right)\sin\left(\sqrt{4\omega_0^2-K_p^2}t\right)\\-4\omega_0^2\end{array}\right]$

The estimated value of the virtual flux vector is shown in Fig. 3, where Ψ_{estimate} is calculated value including steady-state component $\bar{\Psi}$, namely, theoretical value; transient component $\tilde{\Psi}$ shows exponential decay. Therefore, the smaller the absolute value of the transient component is, the smaller the deviation between the estimated value and the theoretical value of the flux vector is. The calculation above shows that different K_p lead to different transient component amplitudes. Suitable K_p needs to be picked out through comparison of transient component amplitudes under three circumstances. Square of amplitude of transient component with different K_p is shown in Table I, which indicates that the amplitude of the transient component is not affected by the phase of initial point, but determined by fundamental frequency ω_0 and resonant filter gain coefficient K_p. In this way, comparison of amplitudes can be converted to comparison of squared amplitudes to simplify the calculation.

Set

$$f_0(t) = \left[2\omega_0^2t^2+2\omega_0t+1\right] * e^{-2\omega_0 t}\ (K_p = 2\omega_0) \quad (26)$$

$$f_1(t) = \frac{e^{-K_p t}}{K_p^2-4\omega_0^2}\left[\begin{array}{l}K_p^2\cosh\left(\sqrt{K_p^2-4\omega_0^2}t\right)\\+K_p\sqrt{K_p^2-4\omega_0^2}\sinh\left(\sqrt{K_p^2-4\omega_0^2}t\right)\\-4\omega_0^2\end{array}\right] \quad (K_p > 2\omega_0) \quad (27)$$

$$f_2(t) = \frac{e^{-K_p t}}{K_p^2 - 4\omega_0^2} \begin{bmatrix} K_p^2 \cos\left(\sqrt{4\omega_0^2 - K_p^2}\,t\right) \\ -K_p\sqrt{4\omega_0^2 - K_p^2}\sin\left(\sqrt{4\omega_0^2 - K_p^2}\,t\right) \\ -4\omega_0^2 \end{bmatrix} \quad (K_p < 2\omega_0). \tag{28}$$

It can be seen that initial values of $f_0(t)$, $f_1(t)$, and $f_2(t)$ are all equal to 1. Deriving $f_0(t)$, $f_1(t)$, and $f_2(t)$, we can obtain the following:

$$f_0'(t) = -4\omega_0^3 t^2 e^{-2\omega_0 t} \tag{29}$$

$$f_1'(t) = \frac{-4K_p\omega_0^2}{K_p^2 - 4\omega_0^2}\left[\cosh\left(\sqrt{K_p^2 - 4\omega_0^2}\,t\right) - 1\right] e^{-K_p t} \tag{30}$$

$$f_2'(t) = \frac{-4K_p\omega_0^2}{K_p^2 - 4\omega_0^2}\left[\cos\left(\sqrt{4\omega_0^2 - K_p^2}\,t\right) - 1\right] e^{-K_p t}. \tag{31}$$

It can be seen from (29)–(31) that $f_0'(t)$, $f_1'(t)$, and $f_2'(t)$ are all less than 0, so $f_0(t)$, $f_1(t)$, and $f_2(t)$ show monotone decreasing.

1) *Compare $f_1(t)$ and $f_0(t)$*

Set

$$g_1(t) = \frac{f'_1(t)}{f'_0(t)}. \tag{32}$$

Both $f_0'(t)$ and $f_1'(t)$ are less than 0, so g_1 is greater than zero. When $g_1 > 1$, the decreasing rate of $f_1(t)$ is greater than that of $f_0(t)$; when $g_1 = 1$, the decreasing rate of $f_1(t)$ equals to that of $f_0(t)$; when $g_1 < 1$, the decreasing rate of $f_1(t)$ is less than that of $f_0(t)$. Via substituting (29) and (30) into (32), the following equation can be derived:

$$g_1(t) = \frac{2K_p}{\omega_0\left(K_p^2 - 4\omega_0^2\right)}\left[\frac{\sinh\left(\frac{\sqrt{K_p^2 - 4\omega_0^2}}{2}t\right)}{t}\right]^2 e^{(2\omega_0 - K_p)t}. \tag{33}$$

Work out the limit value of $g_1(t)$ when t approaches 0, namely

$$\lim_{t\to 0} g_1(t) = \frac{K_p}{2\omega_0} > 1. \tag{34}$$

According to the mathematical theorem, then

$$g_1(t) \approx \frac{2K_p}{\omega_0\left(K_p^2 - 4\omega_0^2\right)}\left[\frac{\frac{\sqrt{K_p^2 - 4\omega_0^2}}{2}t}{t}\right]^2 e^{(2\omega_0 - K_p)t} = \frac{K_p}{2\omega_0} e^{(2\omega_0 - K_p)t}. \tag{35}$$

Set

$$M_1(t) = \frac{K_p}{2\omega_0} e^{(2\omega_0 - K_p)t}. \tag{36}$$

The initial value of $M_1(t)$ equals to $K_p/2\omega_0$ which is greater than 1. When time t approaches positive infinity, $M_1(t)$ equals to zero. In addition, $M_1(t)$ shows monotone decreasing in respect to time t. So, $M_1(t) = 1$ has one and only one positive solution $t1$ shown as follows:

$$t_1 = \frac{1}{2\omega_0}\frac{1}{\frac{K_p}{2\omega_0} - 1}\ln\frac{K_p}{2\omega_0}. \tag{37}$$

Therefore, when $t < t_1$, $M_1(t)$ is less than $K_p/2\omega_0$ and greater than 1; when $t > t_1$, $M_1(t)$ is less than 1 and greater than 0. In this way, when $t > t_1$, $g_1(t)$ is less than 1 and greater than 0.

Set

$$f(x) = \frac{1}{x - 1}\ln x (x > 1) \tag{38}$$

where $x = K_p/2\omega_0$. Work out the limit value of $f(x)$ when x approaches 1 and positive infinity shown as follows:

$$\begin{cases} \lim_{x\to 1} f(x) = 1 \\ \lim_{n\to+\infty} f(x) = 0. \end{cases} \tag{39}$$

$f(x)$ can be derived as follows:

$$f'(x) = \frac{1 - \frac{1}{x} - \ln x}{(x - 1)^2}. \tag{40}$$

Through calculation

$$\lim_{x\to 1} f'(x) = -\frac{1}{2}. \tag{41}$$

When $x > 1$, $f'(x) < 0$, so $f(x)$ shows monotone decreasing, and therefore

$$t_1 < \frac{1}{2\omega_0}. \tag{42}$$

When $t \geq 1/2\omega_0 > t_1$, $g_1(t)$ is less than 1 and greater than 0, and the decreasing rate of $f_1(t)$ is less than that of $f_0(t)$. Through substitution of $t = 1/2\omega_0$ into (30), the following equation can be derived:

$$f_0\left(\frac{1}{2\omega_0}\right) = 0.9197. \tag{43}$$

Since $t = 1/2\omega$ is an extremely small number, the case that the decreasing rate of $f_1(t)$ is greater than that of $f_0(t)$ when $t < t_1$ can be ignored. Therefore, through overall consideration, $f_0(t)$ has better dynamic characteristics than $f_1(t)$.

2) Compare $f_2(t)$ and $f_0(t)$, then (1)–(33) can be derived as follows:

$$f_2'(t) = \frac{-8K_p\omega_0^2}{4\omega_0^2 - K_p^2}\left[\sin\left(\frac{\sqrt{4\omega_0^2 - K_p^2}}{2}t\right)\right]^2 e^{-K_p t}. \tag{44}$$

Therefore

$$f_2'(t) \approx \frac{-8K_p\omega_0^2}{4\omega_0^2 - K_p^2}\left[\frac{\sqrt{4\omega_0^2 - K_p^2}}{2}t\right]^2 e^{-K_p t}. \tag{45}$$

Set a function as $f_3(t)$, and its initial value is the same as $f_0(t)$, $f_1(t)$, and $f_2(t)$ which equals to 1. Its derivative is $f_3'(t)$, shown as follows:

$$f_3'(t) = -2K_p\omega_0^2 t^2 e^{-K_p t}. \tag{46}$$

It can be seen from (41) that the decay rate of $f_3(t)$ is faster than that of $f_2(t)$. Therefore, comparison between $f_2'(t)$ and $f_0'(t)$ can be converted to comparison between $f_3'(t)$ and $f_0'(t)$.

Set

$$M_2(t) = \frac{f'_3(t)}{f'_0(t)}. \tag{47}$$

Substitute (29) and (46) into formula (47), then the following formula can be derived:

$$M_2(t) = \frac{K_p}{2\omega_0} e^{(2\omega_0 - K_p)t}. \tag{48}$$

Since $K_p < 2\omega_0$, $M_2(t)$ shows monotone increasing. When *t* approaches 0 and positive infinity, the limit value of $M_2(t)$ is shown as follows:

$$\begin{cases} \lim_{x\to 0} M_2(t) = \frac{K_p}{2\omega_0} < 1 \\ \lim_{n\to+\infty} M_2(t) = +\infty. \end{cases} \tag{49}$$

So $M_2(t) = 1$ has one and only one positive solution, namely

$$t_2 = \frac{1}{2\omega_0 - K_p} ln \frac{2\omega_0}{K_p}. \tag{50}$$

When $0 < t < t_2$, $M_2(t)$ is less than 1, so the decay rate of $f_0(t)$ is faster than that of $f_3(t)$; when $t > t_2$, $M_2(t)$ is greater than 1, so the decay rate of $f_0(t)$ is slower than that of $f_3(t)$. Equations (1)–(47) can be derived as follows:

$$t_2 = \frac{1}{2\omega_0} \frac{1}{1 - \frac{K_p}{2\omega_0}} \ln \frac{2\omega_0}{K_p}.$$

Set

$$f(x) = \frac{1}{x - 1} \ln x \tag{51}$$

where $x = K_p/2\omega_0$, $0 < x < 1$. Work out the limit value of $f(x)$ when *x* approaches 0 and 1

$$\begin{cases} \lim_{x\to 1} f(x) = +\infty \\ \lim_{n\to 0} f(x) = 1. \end{cases} \tag{52}$$

$f(x)$ can be derived as follows:

$$f'(x) = \frac{1 - \frac{1}{x} - \ln x}{(x - 1)^2}. \tag{53}$$

Through calculation, $f'(x) < 0$, so $f(x)$ shows monotone decreasing. Besides, $f(x)$ equals to 1 when x approaches 1, so $f(x)$ is greater than 1. Thus, t_2 is greater than $1/2\omega_0$. $f_0(1/2\omega_0)$ is proven to be a value approaching 1 after $t = 1/2\omega_0$ is substituted into (1)–(50). Therefore, the time period when $t < t_2$, $M_2(t)$ is less than 1 and the decay rate of $f_0(t)$ is faster than that of $f_3(t)$ can be ignored, which means the decay rate of $f_3(t)$ is faster than that of $f_0(t)$. $f_2(t)$ and $f_3(t)$ are approximate functions based on the previous context. Therefore, through overall consideration, $f_3(t)$ has faster decay rate than $f_2(t)$.

Through comparison, $f_0(t)$ has faster decay rate than $f_1(t)$ and $f_2(t)$ under overall consideration. Thereby, $2\omega_0$ is taken as the gain coefficient K_p of resonant filter with negative feedback.

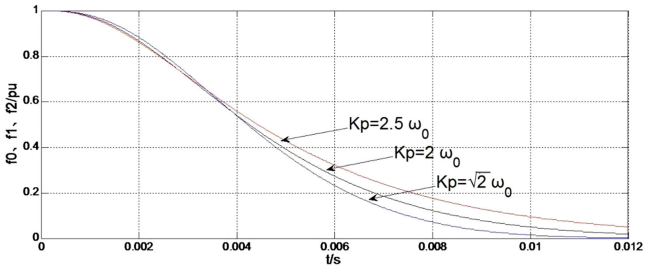

Fig. 4. Simulation waveforms of $f_0(t)$, $f_1(t)$, $f_2(t)$.

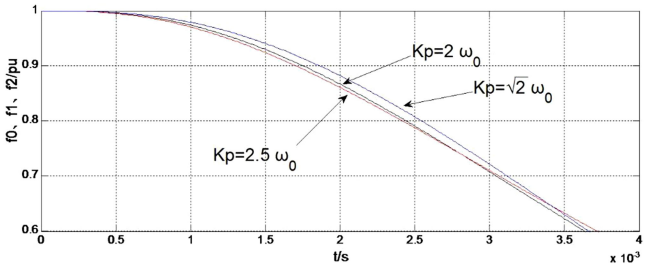

Fig. 5. Simulation waveforms of $f_0(t)$, $f_1(t)$, $f_2(t)$.

From (5), we can obtain the characteristic equation of flux observer with negative feedback

$$s^2 + K_p s + \omega_0^2 = 0. \tag{54}$$

Based on the second-order optimum system of systems engineering, the value of K_p is as follows:

$$K_p = \sqrt{2}\omega_0. \tag{55}$$

When K_p is set as $2\omega_0$, $2.5\omega_0$,$\sqrt{2}\omega_0$, simulation waveforms of corresponding $f_0(t)$, $f_1(t)$, $f_2(t)$ are shown in Fig. 4. Fig. 5 shows the waveforms at initial period of 0–0.0035 s in Fig. 4.

It can be seen from Figs. 4 and 5 that at the initial period, the decay rate of $f_1(t)$ is faster than that of $f_0(t)$, and the decay rate of $f_0(t)$ is faster than that of $f_2(t)$. However, during 0.004 and 0.012 s, the decay rate of $f_0(t)$ is faster than that of $f_1(t)$, and the decay rate of $f_2(t)$ is faster than that of $f_0(t)$. Under overall consideration, the decay rate of $f_2(t)$ is the fastest, which is in line with the previous result.

Virtual flux observer with negative feedback resonant filter not only can solve the time delay caused by one-order low-pass filter, but also has better dynamic characteristics than cascaded structure of dual low-pass filter. Furthermore, its system structure is more favorable to flux observation at uncontrolled rectifying stage.

The system structure of the virtual flux observer with negative feedback resonant filter is shown in Fig. 6. AC-side flux of the rectifier is generated from the integration of ac-side voltage of the rectifier, including fundamental component, harmonic component, and dc component resulting from the integration initial value. With the addition of inductance flux, grid voltage virtual flux and dc bias component can be obtained. Then, accurate grid voltage virtual flux can be obtained by means of resonant filter with negative feedback.

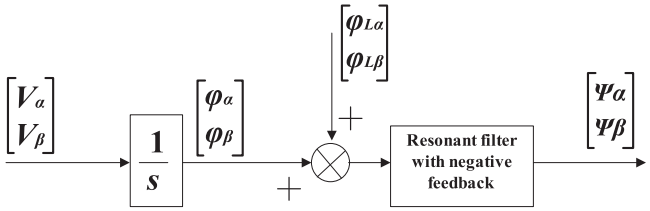

Fig. 6. Resonant filter with negative feedback.

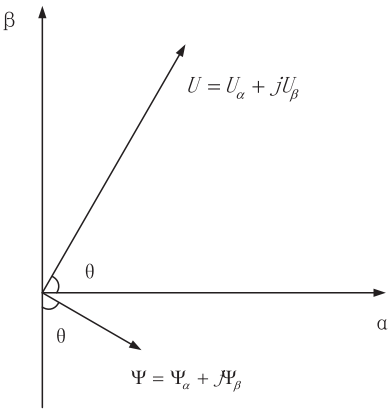

Fig. 7. Voltage reconstruction based on virtual flux.

C. Grid Voltage Reconstruction

Based on the control strategy of inner current control feed-forward decoupling, grid voltage vector will be used to locate and compensate. The algorithm of the virtual flux is presented in Sections II-A and II-B, so grid voltage vector can be obtained indirectly. Equation (3) can be derived as follows:

$$U_\alpha + jU_\beta = -\omega\Psi_\beta + j\omega\Psi_\alpha. \tag{56}$$

The space vector position relation is shown in Fig. 7, which indicates that the amplitude of grid voltage vector is ω time(s) the size of the virtual flux vector, and the phase of grid voltage vector is 90° ahead of the virtual flux vector's phase, therefore

$$\begin{cases} U_\alpha = -\omega\Psi_\beta \\ U_\beta = \omega\Psi_\alpha. \end{cases} \tag{57}$$

According to the transfer matrix shown in (58), combine (57) and (1), then, the component of the grid voltage vector in the *dq* rotating coordinate system is shown in (59)

$$C_{2s2r} = \begin{bmatrix} \cos(\omega t+\theta) & \sin(\omega t+\theta) \\ -\sin(\omega t+\theta) & \cos(\omega t+\theta) \end{bmatrix} \tag{58}$$

$$\begin{bmatrix} U_d \\ U_q \end{bmatrix} = \begin{bmatrix} \omega\sqrt{\Psi_\alpha^2+\Psi_\beta^2} \\ 0 \end{bmatrix}. \tag{59}$$

Based on (1), (58), and (59) in this section, the amplitude of the grid voltage vector and the trigonometric function of the corresponding rotation angle can be figured out, and further applied to double closed-loop current decoupling control.

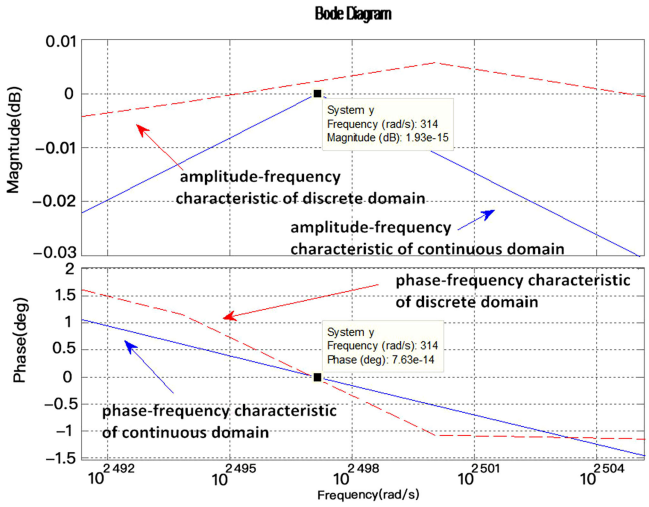

Fig. 8. Bode diagram of filter.

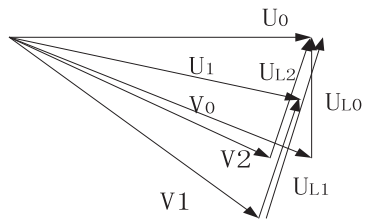

Fig. 9. Voltage vector diagram.

D. Delay Compensation of Virtual Flux Observer

As for the filter of the virtual flux observer, in the case of conversion from continuous complex frequency domain to discrete difference equation, its amplitude-frequency characteristic will change inevitably, and therefore delay will be caused to fundamental signal. Meanwhile, both sampling process and system calculating process may cause delay. Therefore, certain delay exists between the grid voltage vector obtained from the virtual flux and the true value. In this regard, a simple and effective method is proposed in this paper to compensate such delay. The following equation can be obtained after $K_p = 1.414\omega_0$ is substituted into (4)

$$G(s) = \frac{444.221s}{s^2 + 98696.044}. \tag{60}$$

Then, its *Z*-domain formula is as follows:

$$G(z) = \frac{0.02221z^2 - 0.02221}{z^2 - 1.999z + 1}. \tag{61}$$

The Bode diagrams of (59) and (60) is shown in Fig. 8.

When the rectifier runs normally, the actual value of the grid voltage vector is U_0 shown as Fig. 9. After controlling by the unity power factor, the grid voltage vector and ac-side voltage vector of the rectifier bridge are U_{L0} and V_0, respectively. The observed voltage vector is U_1 which has θ_{rad} delay compared to the phase of U_0 By using the double-loop control, if we want the dc-side voltage equal to the set value, then the inductance voltage vector is shown as U_{L2}, whose component is U_{L0} in the vertical direction. Besides, due to the unity power factor

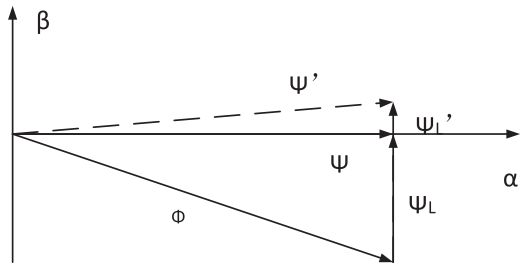

Fig. 10. Compensation of virtual flux delay.

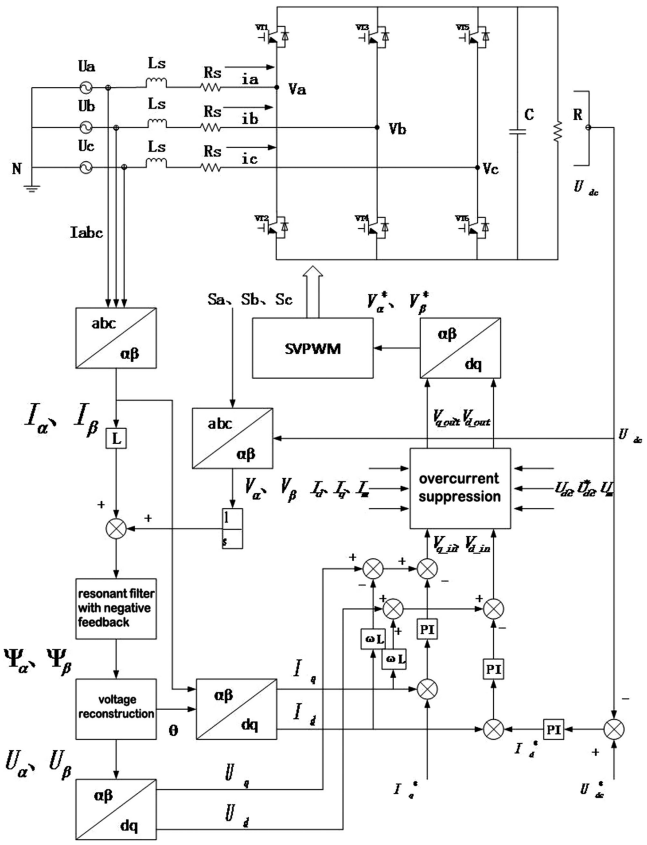

Fig. 11. Diagram of control system of rectifier without grid voltage sensor based on virtual Flux.

control, U_{L2} is perpendicular to U_1. V_2 is the output fundamental frequency voltage vector of the rectifier bridge. Through U_{L2} and V_2, we can theoretically calculate U_0. However, influenced by the system sampling, modulation delay and the changing of filter from continuous domain to discrete domain, the calculated voltage is U_1, while V_1 is the equivalence of rectifier bridge's ac-side voltage vector after delayed. Thus, we use U_{L2} instead of U_{L1} to obtain U_0. U_{L1} can be used to replace U_{L2} to obtain U_0

$$K = \frac{U_{L1}}{U_{L2}} = \frac{2U_{L2} - V_{2\beta}}{U_{L2}} = 2 - \frac{V_{2\beta}}{U_{L2}} \tag{62}$$

where $V_{2\beta}$ is the component of V_2 in βaxle in the two-phase stationary $\alpha\beta$ coordinate system; U_{L1} is the inductance voltage;

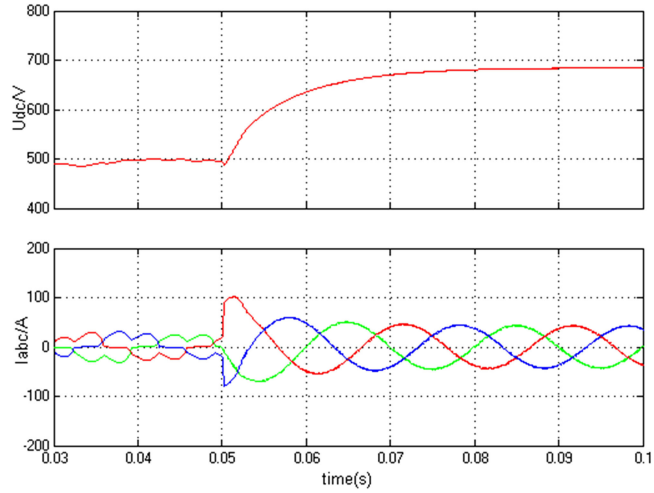

Fig. 12. DC-side voltage and ac-side current.

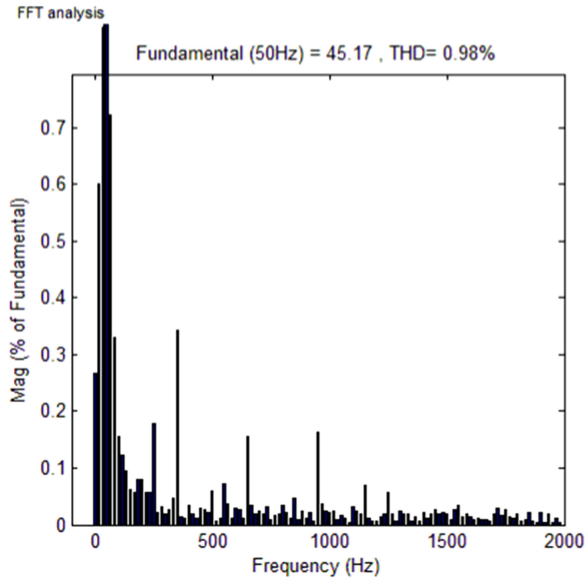

Fig. 13. Harmonic analysis of a phase current.

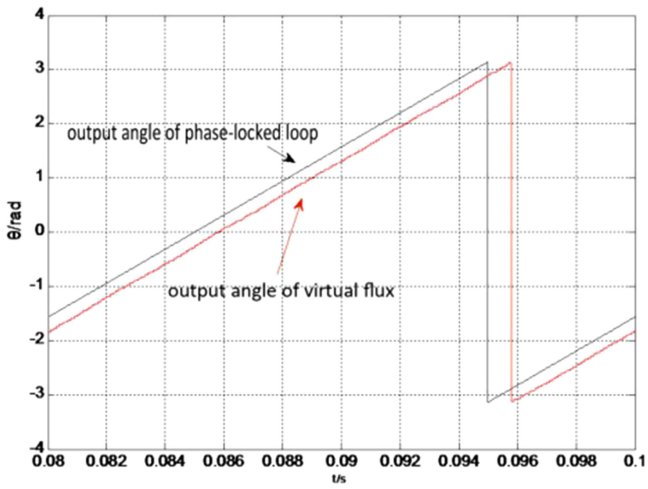

Fig. 14. Output angle of phase-locked loop and that of virtual flux during uncontrolled rectifier.

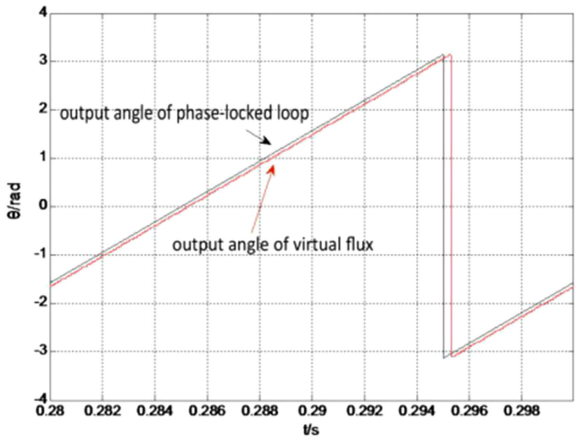

Fig. 15. Output angle of phase-locked loop and that of virtual flux during controlled rectifier.

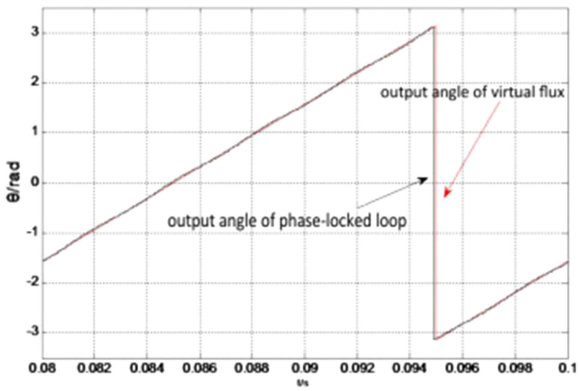

Fig. 16. Output angle of phase-locked loop and that of virtual flux during uncontrolled rectifier after compensation.

U_{L2} denotes the actual inductance voltage. Since the frequency remains unchanged, the equivalent inductance is shown as follows:

$$L_{eq} = KL_{re}. \tag{63}$$

In this paper, the proposed delay compensation method is designed to adjust inductance used for the calculation of virtual flux and further adjust the phase of virtual flux. The adjustment effect is shown in Fig. 10, in which, Ψ is the virtual flux of the grid voltage, Ψ_L is the virtual flux of inductance partial pressure, and Φ is the virtual flux of the ac-side voltage of rectifier. When the rectifier runs as per unity power factor, Ψ_L is perpendicular to Ψ. After fine adjustment of Ψ_L, it becomes $\Psi_L\prime$, and corresponding virtual flux of grid voltage turns out to be Ψ'. In this way, delay can be compensated while little change happens to flux amplitude.

E. PWM Rectifier Control System Without Grid Voltage Sensor Based on Virtual Flux

According to the analysis and calculation of the virtual flux algorithm in Sections II-A, II-B, II-C, and II-D of this paper, the diagram of the PWM rectifier control system without grid voltage sensor based on virtual flux can be obtained, as shown in Fig. 11.

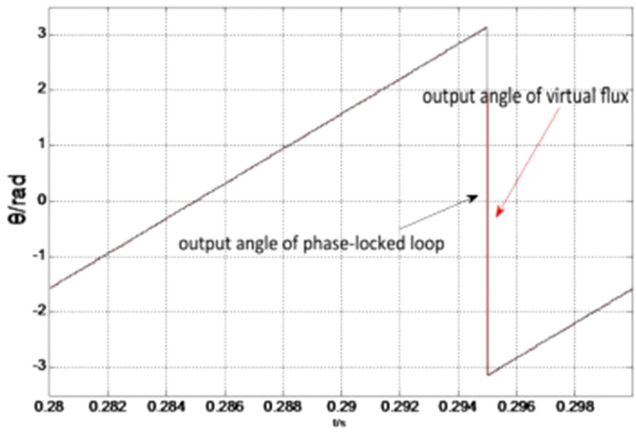

Fig. 17. Output angle of phase-locked loop and that of virtual flux during controlled rectifier after compensation.

(a) (b)

Fig. 18. Experimental platform. (a) Three-phase two-level PWM rectifier experimental platform. (b) Controller.

TABLE II
SIMULATION PARAMETERS

Parameter/Unit	Value
Rated power/kW	20
Line voltage/V	380
Rated current I_N/A	30
Rated frequency /Hz	50
DC side voltage given /V	680
Switching frequency /kHz	5

III. SIMULATION RESEARCH

A. Parameters of Simulation Model

Combined with the system structure and algorithm implementation method in previous sections, simulation is carried

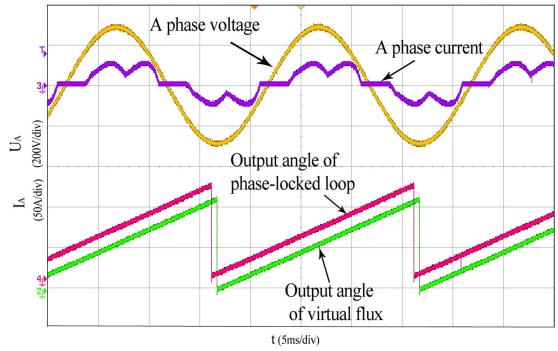

Fig. 19. Output angle of phase-locked loop and that of virtual flux at uncontrolled rectifying stage.

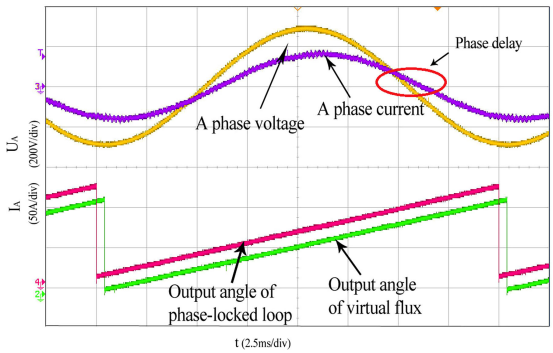

Fig. 20. Output angle of phase-locked loop and that of virtual flux at controllable rectifying stage.

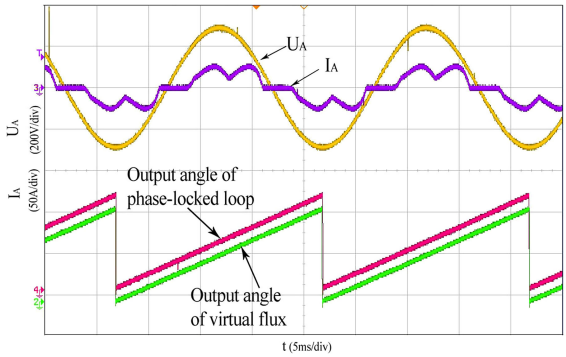

Fig. 21. Output angle of phase-locked loop and that of virtual flux at uncontrolled rectifying stage after delay compensation.

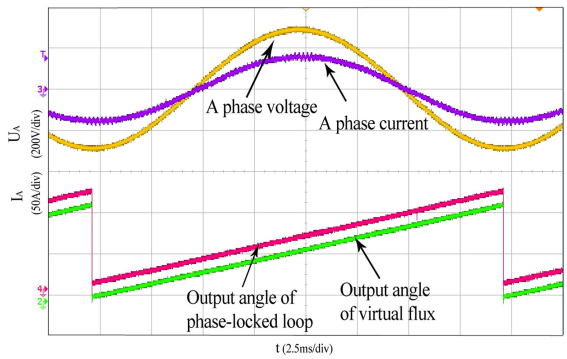

Fig. 22. Output angle of phase-locked loop and that of virtual flux at controllable rectifying stage after delay compensation.

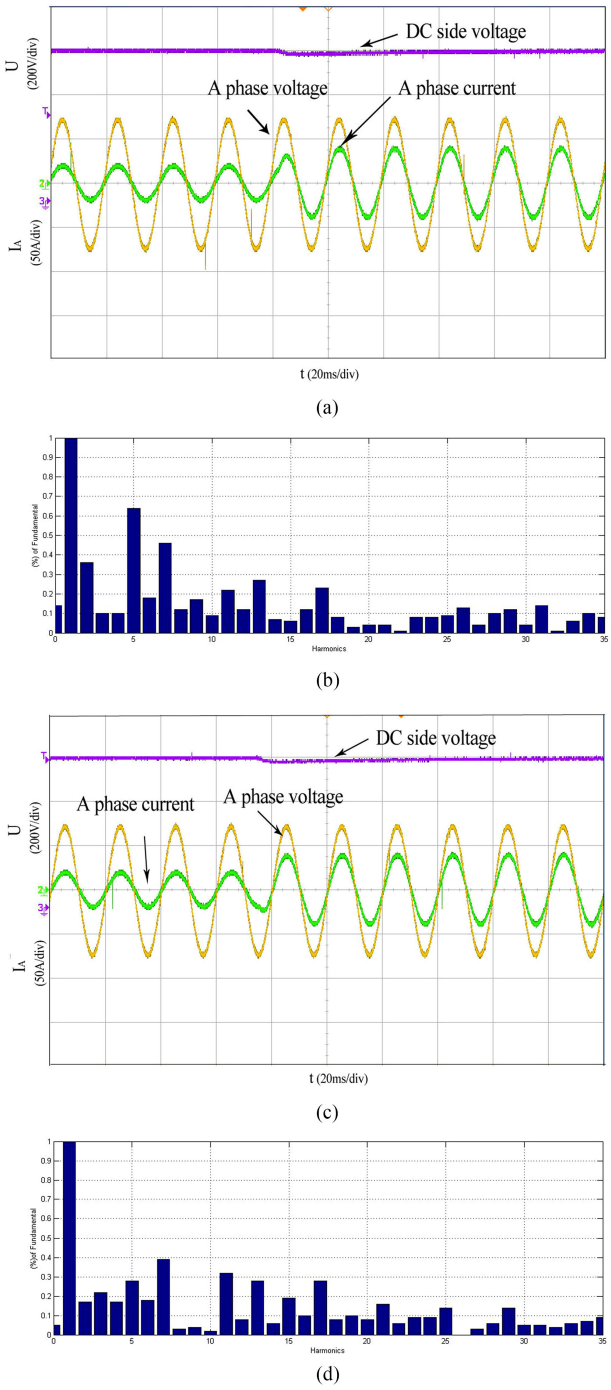

Fig. 23. Waveforms at the time of load sudden change. (a) Experimental result of PWM rectifier without voltage sensor. (b) Harmonic analysis of a phase current without voltage sensor in steady state and the THD is 1.18%. (c) Experimental result of PWM rectifier with voltage sensor. (d) Harmonic analysis of a phase current with voltage sensor in steady state and the THD is 1.03%.

out to verify the PWM rectifier without grid voltage sensor in accordance with set simulation parameters.

B. Result of Simulation

As for the PWM rectifier without network voltage sensor, its dc-side voltage and ac-side current are shown in Fig. 12.

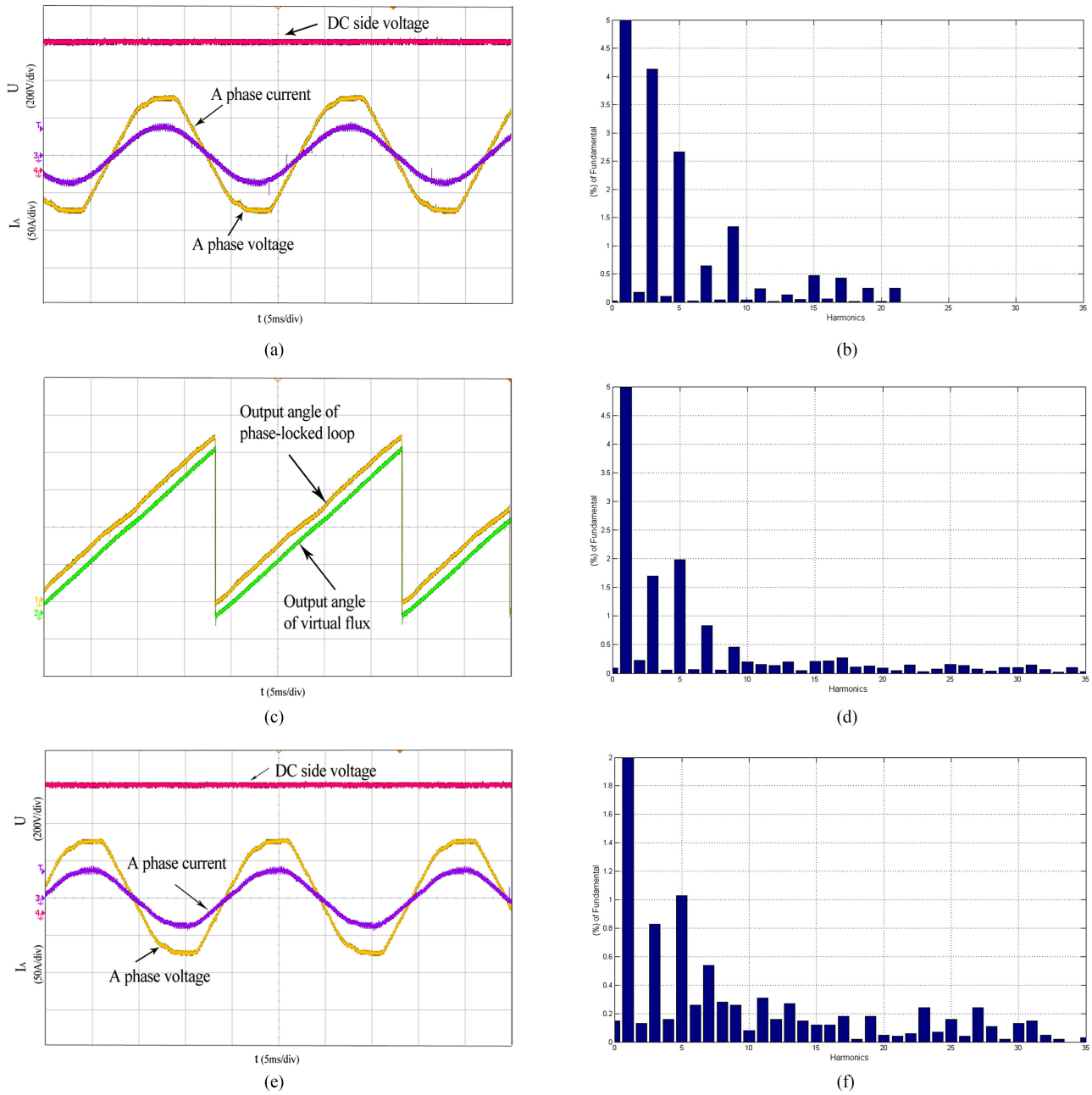

Fig. 24. Experimental result of PWM rectifier with harmonic of the grid voltage. (a) Phase voltage and current oscillogram of PWM rectifier without voltage sensor. (b) Harmonic analysis of A phase grid voltage and the THD is 5.2%. (c) Output angles of phase-locked loop and that of virtual flux. (d) Harmonic analysis of A phase current without voltage sensor and the THD is 4.06%. (e) Phase voltage and current oscillogram of PWM rectifier with voltage sensor. (f) Harmonic analysis of a phase current with voltage sensor and the THD is 3.36%.

It can been seen from the figure that after the rectifier reaches steady state, the dc-side voltage is under effective control and the ac-side current realizes three-phase symmetry, with high degree of sine. Harmonic analysis of a phase current is shown in Fig. 13, which indicates that total harmonic distortion of a phase THD = 0.98%, with small harmonic content.

The comparison between the output angle of phase-locked loop with sensor and that of the virtual flux observer without sensor at uncontrolled rectifying stage is shown in Fig. 14, which indicates that it can realize flux observation and voltage reconstruction at the uncontrolled rectifying stage, but there is certain delay compared to the algorithm with sensor. The comparison between the output angle of phase-locked loop with sensor and that of the virtual flux observer without sensor at controllable rectifying stage is shown in Fig. 15, which indicates that it can realize virtual flux observation and voltage reconstruction at controllable rectifying stage, but there is also certain delay compared to the algorithm with sensor. After compensation of the virtual flux delay, the observation result at the uncontrolled rectifying stage and the output result of the phase-locked loop with sensor are shown in Fig. 16, which indicate that the time delay between the former and the latter can be ignored. The

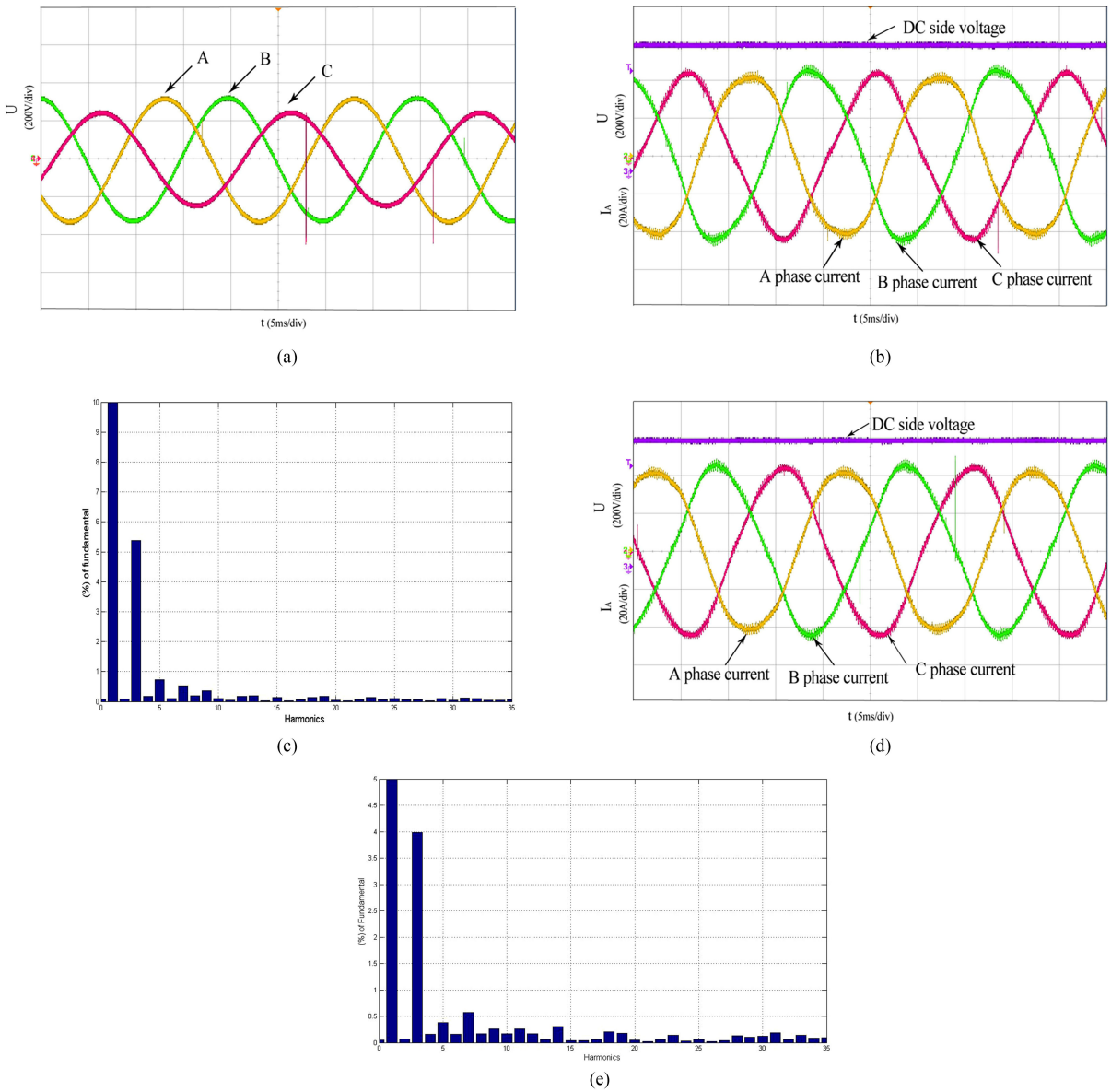

Fig. 25. Experimental results of PWM rectifier when one phase of the grid voltage drops. (a) Three-phase grid voltage waveforms. (b) Three-phase current waveform without voltage sensor. (c) Harmonic analysis of A phase current without voltage sensor and the THD is 5.51%. (d) Three-phase current waveform with voltage sensor. (e) Harmonic analysis of a phase current with voltage sensor. THD is 4.15%.

observation result at the controllable rectifying stage and the output result of phase-locked loop with sensor are shown in Fig. 17, which indicate that the delay between the former and the latter can be ignored as well. According to Figs. 14–17, flux angle can be correctly observed through algorithm of virtual flux, and the delay can be appropriately compensated through algorithm of delay compensation.

IV. Experiment Research

A. Experimental Verification

The algorithm proposed in this paper is verified through the experimental platform of three-phase two-level PWM rectifier, which is shown in Fig. 18. Experimental parameters are consistent with simulation parameters as shown in Table II. Key controllers of the experiment include TMS320F28335 DSP of Texas Instruments and Spartan- XC6SLX45 FPGA of Xilinx. DSP completes core algorithm as the main controller, and FPGA completes AD sampling, dead zone delay, and other miscellaneous functions as the coprocessor. 7MBP150RA120 IPM is used as the IGBT power module. In order to facilitate measurement, semaphore to be measured was observed by Agilent MSO6014A oscilloscope through D/A output.

B. Experimental Results

Without algorithm of the virtual flux compensation, the observation angle of virtual flux at the uncontrolled rectifying stage and the output angle of phase-locked loop with sensor are shown in Fig. 19, which indicate that the delay exists between the output angle of virtual flux and that of the phase-locked loop; the

observation angle of virtual flux at the controllable rectifying stage and the output angle of phase-locked loop with sensor is shown in Fig. 20, which indicates that the delay exists between the output angle of virtual flux and that of the phase-locked loop as well. After delay compensation, the observation angle of virtual flux at the uncontrolled rectifying stage and the output angle of the phase-locked loop with sensor are shown in Fig. 21, which indicate that delay between the output angle of virtual flux and that of the phase-locked loop can be ignored; the observation angle of virtual flux at the controllable rectifying stage and the output angle of the phase-locked loop with sensor is shown in Fig. 22, which indicates that delay between the output angle of virtual flux and that of the phase-locked loop can be ignored as well.

Fig. 23 shows the voltage waveform at the time of load sudden change. The set value of voltage is 720 V, and initial load resistance is 16 Ω. During steady state, the voltage waveform can perfectly follow set value, current waveform and voltage waveform have the same phase, and current is approximately sine wave. It can be seen from the figure that during the transient process, voltage and current always have the same phase, without vibrating phenomenon. Fig. 23(b) and (d) show that THD of grid current is 1.18% and 1.03%, respectively. From the experimental result, it can be seen that the algorithm proposed in this paper can achieve the same control effect as the PWM rectifier with voltage sensor.

In actual field operation, the use of various nonlinear loads would result in nonstandard three-phase grid voltage. The grid voltage may be distorted to generate different higher harmonics. Thus, to ensure the sound operation of control algorithm when the grid voltage is distorted is very necessary. In this experiment, the three-phase voltage source in the laboratory is used to power the converter. The single-phase voltage amplitude of the three-phase voltage source is 334 V. Fig. 24(b) shows that THD is 5.2% including three-time, five-time, and seven-time and other odd harmonics.

Fig. 24 shows that after grid voltage is distorted, when adopting the method with voltage sensor, the grid current THD has risen to 3.36% from 1.03%, while adopting the method without voltage sensor, the grid current THD has risen from 1.18% when the grid voltage is not distorted to 4.06%. From Fig. 24(c), the time delay of the output angle of virtual flux relative to the phase-locked loop can also be ignored. Hence, when the grid voltage is distorted, the algorithm proposed in this paper can ensure a sound sine degree of grid output current and achieve the same control effect as the algorithm with voltage sensor.

In a real industrial application environment, when a power system is short circuited, or a high-power nonlinear load is switched ON, it may cause a transient drop of one phase of the three-phase power supply. Therefore, it is valuable to ensure the steady and normal function of the algorithm when one-phase voltage drops and keeps the converter from withdrawing the system.

Fig. 25 is the experimental oscillogram of two algorithms when A phase voltage drops 25%. It can be seen from the figure, when the grid voltage drops, the proposed algorithm can keep the three-phase symmetry of three-phase grid output current, and achieve the same control effect as the algorithm with voltage sensor, which can guarantee the normal operation and good reliability of the system.

V. Conclusion

Mathematical model of the virtual flux algorithm is analyzed in this paper. The improvement is made to the existing virtual flux observer, and then the virtual flux observer with negative feedback resonant filter is proposed in this paper. The simulation and experimental results show that the proposed virtual flux observer can realize flux estimation without steady-state error and it has better dynamic characteristics than the series algorithm of dual low-pass filter. Furthermore, relevant parameters of the observer are adjusted. Eventually, a delay compensation algorithm is brought forward to solve the delay of virtual flux, which can effectively compensate the error caused by system delay to flux observation. In this paper, the aging of electric reactor is not taken into account. The estimated value of the virtual flux is bounded to change with the change of inductance.

References

[1] C.-J. Zhang *et al.*, "A novel virtual space vector modulation strategy for the neutral-point potential comprehensive balance of neutral-point-clamped converters," *J. Power Electron.*, vol. 16, no. 3, pp. 946–959, May 2016.

[2] H. Zhang *et al.*, "Voltage vector error fault diagnosis for open-circuit faults of three-phase four-wire active power filters," *IEEE Trans. Power Electron,* vol. 32, no. 3, pp. 2215–2226, Mar. 2017.

[3] S. Eren, M. Pahlevaninezhad, A. Bakhshai, and P. Jain, "Grid-connected voltage source inverter for renewable energy conversion system with sensorless current control," in *Proc. 25th Annu. IEEE Appl. Power Electron. Conf. Expo.*, 2010, vol. 1, pp. 768–772.

[4] H.-C. Chen and C. Yu Lu, "Digital current sensorless control for dual-boost half-bridge PFC converter with natural capacitor voltage balancing," *IEEE Trans. Power Electron*, vol. 32, no. 5, pp. 4074–4083, May 2017.

[5] K. Kant1 and S. R. Arya, "Current sensorless control algorithm of DSTATCOM for power quality improvement," in *Proc. Annu. IEEE India Conf.*, Dec. 2015, pp. 2325–9418.

[6] J. Gonzalez Norniella *et al.*, "Improving the dynamics of virtual-flux-based control of three-phase active rectifiers," *IEEE Trans. Ind. Electron.*, vol. 61, no. 2, pp. 177–187, Jan. 2014.

[7] M. B. Ketzer and C. B. Jacobina, "Nonlinear virtual flux oriented control for sensorless active filters," in *Proc. Power Electron. Conf.,* Oct. 2013, pp. 393–398.

[8] M. Razali, M. A. Rahman, and N. A. Rahim, "Real-time implementation of d-q control for grid connected three phase voltage source converter," in *Proc. 40th Annu. Conf. IEEE Ind. Electron. Soc.*, Oct./Nov. 2014, pp. 1733–1739.

[9] M. B. Ketzer and C. B. Jacobina, "Sensorless control technique for PWM rectifiers with voltage disturbance rejection and adaptive power factor," *IEEE Trans. Ind. Electron.*, *vol.* 62, no. 2, pp. 1140–1151, Feb. 2015.

[10] K. Sahraoui1, K. Sahraoui1, and L. Mokrani, "Fault tolerant control of redundant topology of PWM AC-DC-AC converter supplying an electromechanical drive," in *Proc. 8th Int. Conf. Model., Identification Control*, Nov. 2016, pp. 374–380.

[11] J. A. Suul, A. Luna, P. Rodríguez, and T. Undeland, "Voltage-sensor-less synchronization to unbalanced grids by frequency-adaptive virtual flux estimation," *IEEE Trans. Ind. Electron.*, vol. 59, no. 7, pp. 2910–2923, Jul. 2012.

[12] J. Hu and B. Wu, "New integration algorithms for estimating motor flux over a wide speed range," *IEEE Trans. Power Electron.*, vol. 13, no. 5, pp. 969–977, Sep. 1998.

[13] W. C. A. Pereira *et al.*, "Improved sensorless vector control of induction motor using sliding mode observer, " *IEEE Latin Amer. Trans.,* vol. 14, no. 7, pp. 3110–3116, Jul. 2016.

[14] Ai-L. Zhang and X. Wang, "A static two-axis model and its application in direct torque control system for brushless doubly fed induction machine," in *Proc. 9th Int. Conf. Power Electron. Drive Syst.,* Dec. 2011, pp. 968–973.
[15] M. Comanescu and L. Xu, "An improved flux observer based on PLL frequency estimator for sensorless vector control of induction motors," *IEEE Trans. Ind. Electron.*, vol. 53, no. 1, pp. 50–56, Feb. 2006.
[16] D. Kouchih, R. Hachelaf, N. Boumalha, M. Tadjine, and M. S. Boucherit, "Improvement of sensorless vector controlled induction motor drives using a new algorithm for the rotor resistance adaptation," in *Proc. 5th Int. Conf. Syst. Control*, Jul. 2016*,* pp. 67–71.
[17] M. Cirrincione, M. Pucci, G. Cirrincione, and G. A. Capolino, "A new adaptive integration methodology for estimating flux in induction machine drives," *IEEE Trans. Power Electron.*, vol. 19, no. 1, pp. 25–34, Jan. 2004.
[18] C. Patel, R. Ramchand, K. Sivakumar, A. Das, and K. Gopakumar, "A rotor flux estimation during zero and active vector periods using current error space vector from a hysteresis controller for a sensorless vector control of IM drive," *IEEE Trans. Ind. Electron.*, vol. 58, no. 6, pp. 2334–2344, Jun. 2011.
[19] T. Guojun, W. Xuanqin, Z. Yanping, and Z. Liang, "Study on sensorless control strategy of multi-level PWM rectifier based on a novel virtual flux observer," in *Proc. Asia-Pac. Power Energy Eng. Conf.*, Apr. 2010, pp. 1–4.
[20] B. Q. Van Ngo, P. Rodriguez-Ayerbe, S. Olaru, and S.-I. Niculescu, "Model predictive power control based on virtual flux for grid connectedthree-level neutral-point clamped inverter," in *Proc. 18th Eur. Conf. Power Electron. Appl.*, Oct. 2016, pp. 1–10.
[21] M. Hu and L. Wu, "Improved virtual flux-oriented model predictive-power control of grid inverters," in *Proc. 10th Conf. Ind. Electron. Appl.,* Nov. 2015, pp. 111–1113.
[22] N. F. Roslan, J. A. Suul, and A. Luna, "A simulation study of proportional resonant controller based on the implementation of frequency adaptive virtual flux estimation with the LCL filter," in *Proc. 41st Annu. Conf. IEEE Ind. Electron. Soc.,* Nov. 2015, pp. 1934–1941.
[23] M. B. Ketzer and C. B. Jacobina, "Virtual flux sensorless control for shunt active power filters with quasi-resonant compensators," *IEEE Trans. Power Electron.*, vol. 31, no. 7, pp. 4818–4830, Jul. 2006.
[24] M. Ketzer and C. Jacobina, "Sensorless control technique for PWMrectifiers with voltage disturbance rejection and adaptive power factor," *IEEE Trans. Ind. Electron.*, vol. 62, no. 2, pp. 1140–1151, Feb. 2015.
[25] P. Dai, Su Dong, X. Fu, and Y. Li, "Vector control of PWM rectifier based on a novel virtual flux observer," in *Proc. Int. Conf. Mechatronics Autom.*, Aug. 2011, pp. 1641–1645.
[26] Wu Fengjiang, W. Zhiwen, and S. Li, "Improved virtual flux oriented-vector control of PWM rectifier," *Elect. Mach. Control*, vol. 12, no. 5, pp. 504–508, Aug. 2008.
[27] Z. Yingchao, J. Liping, Z. Yongchang, Lu Ting, and Z. Zhengming, "Virtual flux based direct power control for three-level PWM rectifier," in *Proc. 17th Int. Conf. Elect. Mach. Syst.*, Oct. 2014, pp. 1441–1446.
[28] M. B. Ketzer and C. B. Jacobina, "Sensorless control technique for PWM rectifiers with voltage disturbance rejection and adaptive power factor," *IEEE Trans. Ind. Electron.*, vol. 62, no. 2, pp. 1140–1151, Feb. 2015.
[29] M. B. Ketzer and C. B. Jacobina, "Sensorless current shaping control technique for shunt active filters," in *Proc. 11th IEEE/IAS Int. Conf. Ind. Appl.*, Mar. 2014, pp. 7–10.

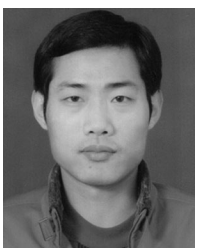

Hui Zhang was born in Xuzhou, China, in October 1983. He received the B.S. degree in electrical engineering and the Ph.D. degree in power electronics and electrical drives from China University of Mining and Technology, Xuzhou, China, in 2006 and 2011, respectively.

He is currently a Lecturer of power electronics and electrical drives with the School of Electrical and Power Engineering, China University of Mining and Technology. His current research interests include power electronics, power quality compensation systems, and motor control.

Xiaoxiao Zhu was born in Lianyungang, China, in January 1994. She received the B.S. degree in electrical engineering from Qingdao University of Technology, Qingdao, China, in 2015. She is currently working toward the M.S. degree in electrical engineering at the China University of Mining and Technology, Xuzhou, China.

Her current research interests include PWM rectifier control strategy and MMC control strategy.

Jingcong Shi was born in Xuzhou, China, in August 1989. He received the B.S. and M.S. degrees in electrical engineering from China University of Mining and Technology, Xuzhou, China, in 2012 and 2016, respectively.

He is currently an Assistant Engineer with NO.704 Research Institute, China Shipbuilding Industry Corporation, Shanghai, China. His current research interests include power electronics, power quality compensation systems, and motor control.

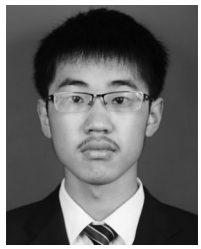

Li Tan was born in Chenzhou, China, in August 1994. He received the B.S. degree in electrical engineering from China University of Mining and Technology, Xuzhou, China, in 2016. He is currently working toward the M.S. degree in electrical engineering from China University of Mining and Technology.

His current research interests include PWM rectifier, power quality compensation systems, and power electronics.

Chuanjin Zhang was born in Xuzhou, China, in November 1986. He received the B.S. degree in electronic information science and technology from Northeast Dianli University, Jilin, China, in 2009, and the M.S. degree in power electronics and drives and the Ph.D. degree in electrical engineering from China University of Mining and Technology, Xuzhou, China, in 2012 and 2017, respectively.

He is currently a Lecturer with Jiangsu Vocational Institute of Architectural Technology, Xuzhou, China. His current research interests include power quality compensation systems, motor control, and power electronics.

Kun Hu was born in Xuzhou, China, in April 1978. He received the B.S. degree in electrical engineering and its automation, the M.S. and Ph.D. degrees in power electronics and power drives from China University of Mining and Technology, Xuzhou, China, in 2000, 2007, and 2014, respectively.

He is currently an Associate Professor with the School of Electrical and Power Engineering, China University of Mining and Technology. His current research interests include design of new type of motors, electric machines, and electric apparatus.